Ab initio study of the vibrational properties of crystalline TeO_2: The α, β, and γ phases

M. Ceriotti, F. Pietrucci, and M. Bernasconi
Dipartimento di Scienza dei Materiali, Università di Milano-Bicocca, Via Cozzi 53, I-20125, Milano, Italy
(Received 29 November 2005; revised manuscript received 24 January 2006; published 28 March 2006)

Based on density functional perturbation theory, we have studied the vibrational properties of three crystalline phases of tellurium dioxide: paratellurite α-TeO_2, tellurite β-TeO_2, and the new phase γ-TeO_2, recently identified experimentally. Calculated Raman and IR spectra are in good agreement with available experimental data. The vibrational spectra of α- and β-TeO_2 can be interpreted in terms of vibrations of TeO_2 molecular units.

DOI: 10.1103/PhysRevB.73.104304 PACS number(s): 78.30.−j, 61.50.Ah, 63.20.Dj, 71.15.Mb

I. INTRODUCTION

Tellurium oxide (TeO_2) and TeO_2-based glasses are promising active materials for optical switching devices due to their large nonlinear polarizability[1] and for optical amplifiers due to their large cross section for stimulated Raman scattering (SRS).[2,3] Three crystalline phases of TeO_2 are well documented. The paratellurite α-TeO_2 (Ref. 4) and the tellurite β-TeO_2 (Ref. 5) phases have been known for a long time. Recently, a third crystalline polymorph metastable at normal conditions, γ-TeO_2,[6,7] has been identified by x-ray powder diffraction of recrystallized tellurite glasses doped with metal oxides. The three phases can be described as different arrangements of corner-sharing TeO_4 units (the distorted trigonal bipyramids in Fig. 1). These units have two longer Te-O bonds (axial bonds) and two shorter ones (equatorial bonds) whose length varies in the different phases. Paratellurite, α-TeO_2, has a three-dimensional fully connected structure, while β-TeO_2 has a layered structure with weakly bonded sheets. In γ-TeO_2, one Te−O bond is substantially larger than the other three and by breaking this bond in a three-dimensional visualization of the network, a chainlike structure appears. The γ-TeO_2 phase has then been described in terms of a polymeric form made of TeO_3 units.[6,7] By comparing the Raman spectra of TeO_2 glasses with those of the crystalline phases, it has also been proposed that the chainlike structure of γ-TeO_2 would represent the main structural feature of the glass.[8] Theoretical lattice dynamics calculations of the phonon spectra of crystalline TeO_2 have already appeared in the literature,[7–11] based on empirical interatomic force constants from two- and three-body interactions or shell models.[9] The lattice dynamics calculations revealed that the phononic spectra of α-TeO_2 and β-TeO_2 can be well interpreted in terms of vibrations of weakly coupled TeO_2 molecules.[7,8,10,11] Accordingly, tellurite and paratellurite would be seen as molecular crystals made of TeO_2 molecules. The polymeric γ-TeO_2 would represent a chainlike polymerization of TeO_2 molecules giving rise to a structure more connected than the paratellurite and tellurite phases.

In this paper, we investigate further the three crystalline phases of TeO_2 (α, β, γ) by computing their structural and vibrational properties from first principles. We aim at providing a compelling assignment of the experimental Raman and IR peaks to specific phonons which would allow one to identify the vibrational signature of the different structural units in the crystals and in the glass.

After a brief description of our theoretical framework in Sec. II, we present our results on the structural and electronic properties in Sec. III and on the vibrational properties in Sec. IV. Section V reports our conclusions.

II. COMPUTATIONAL DETAILS

Calculations are performed within the framework of density functional theory (DFT) within the simple local density approximation (LDA) and with gradient-corrected exchange and correlation energy functionals [Perdew-Burke-Ernzerhof[12] (PBE) and Becke-Lee-Yang-Parr[13] (BLYP)], as implemented in the codes PWSCF and PHONONS.[14] Calculations are performed with ultrasoft pseudopotentials.[15] Kohn-Sham orbitals are expanded in a plane-wave basis up to a kinetic cutoff of 30 Ry. Brillouin zone (BZ) integration has been performed over Monkhorst-Pack meshes of $8\times8\times8$, $4\times4\times4$, and $6\times6\times6$ k-points for α-, β-, and γ-TeO_2, respectively.[16] Equilibrium geometries have been obtained by optimizing the internal and lattice structural parameters at several volumes and fitting the energy versus volume data with a Murnaghan function.[17] Residual anisotropy in the stress tensor at the optimized lattice parameters at each volume is below 0.6 kbar. Infrared and Raman spectra are obtained from effective charges, dielectric susceptibilities, and phonons at the Γ point within density functional perturbation

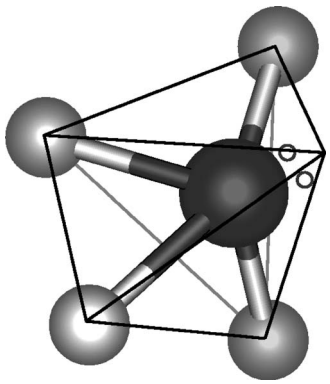

FIG. 1. The TeO_4 bipyramidal unit, building block of the three TeO_2 polymorphs. The two small circles indicate the Te lone pair. Dark (light) spheres indicate Te (O) atoms.

TABLE I. Bond length, bond angle, and vibrational frequencies of TeO_2 molecule, compared with previous B3LYP (Ref. 34) and experimental (Ref. 35) data. B_1 and $A_1(2)$ are antisymmetric and symmetric stretching modes, respectively, while $A_1(1)$ is a bending mode of the TeO_2 molecule.

			ω (cm^{-1})		
	Te-O (Å)	Te-O-Te (deg)	$A_1(1)$	$A_1(2)$	B_1
PBE	1.832	111.7	266	804	806
BLYP	1.820	111.8	265	813	824
B3LYP	1.844	112.9	250	883	921
Expt.	1.840	112	294	810	849

theory.[18] Effective charges have been computed with norm-conserving pseudopotentials[19] and a kinetic cutoff of 70 Ry. Relevant formula for the calculation of the IR and Raman spectra are given in Sec. IV. Preliminary tests on the transferability of the pseudopotentials and on the accuracy of the exchange and correlation functionals have been performed on the structure and vibrational frequencies of the TeO_2 molecule. Results are presented in Table I for PBE and BLYP functionals and compared with experimental data and previous B3LYP all-electron calculations.

III. STRUCTURAL PROPERTIES

A. α-TeO_2

The paratellurite crystal (space group $P4_12_12$, D_4^4, no. 92) has tetragonal symmetry with four formula units per unit cell.[4] Two atoms are independent by symmetry: one Te atom at position $(x,x,0)$ and one oxygen atom at position (α,β,γ). The experimental and theoretical (LDA and PBE) lattice parameters and positions of the symmetry-independent atoms are given in Table II. As usual the LDA [generalized gradient approximation (GGA)] underestimates (overestimates) the equilibrium volume with respect to experimental data. The bulk modulus and its derivative with respect to pressure obtained from the fitted Murnaghan equation of state (PBE functional) are $B=33.0$ GPa and $B'=8.1$ to be compared with the experimental value of $B=45.3$ GPa.[20] These results are in good agreement with previous all-electron calculations, which confirms the transferability of our pseudopotentials.[21] Concerning the internal structure of α-TeO_2, a Te atom is coordinated with four oxygen atoms, two equatorial atoms at closer distance (expt. 1.88 Å) and two axial atoms at larger distance (expt. 2.12 Å).[4] The structure can be seen as a network of corner-sharing TeO_4 units (Fig. 2), the oxygen atoms bridging two Te atoms. The network is formed by six-membered rings of Te atoms with bridging oxygen atoms. As already mentioned, lattice dynamics calculations with empirical interatomic potentials suggest an alternative picture of α-TeO_2 as formed by weakly interacting TeO_2 molecules.[8,10,11] The calculated independent bond lengths and angles are compared with experimental data in Table III for LDA and PBE functionals at the theoretical equilibrium lattice parameters, and for PBE and BLYP functionals at the experimental lattice parameters. Although the error in the lattice parameters is within the expected accuracy for DFT calculations, the error in the bond lengths at the theoretical lattice parameters is somehow larger than usual (cfr. Table III). In particular the calculated equatorial and axial Te-O bond lengths are much closer to each other than in the experimental structure. This misfit is

TABLE II. Structural parameters of α-TeO_2, calculated with LDA functional, with PBE functional at the theoretical (PBE) and experimental (PBE expt.) lattice parameters, and with BLYP functional at the experimental lattice parameters (BLYP expt.). Experimental x-ray data (Expt.) are from Ref. 4.

	LDA	PBE	PBE expt.	BLYP expt.	Expt.
			Cell parameters (Å)		
a	4.819	4.990			4.8082
c	7.338	7.546			7.612
			Atomic positions		
Te x	0.0025	0.0272	0.0156	0.0201	0.0268
O α	0.1402	0.1467	0.1371	0.1388	0.1368
O β	0.2379	0.2482	0.2492	0.2519	0.2576
O γ	0.2065	0.1968	0.1954	0.1926	0.1862

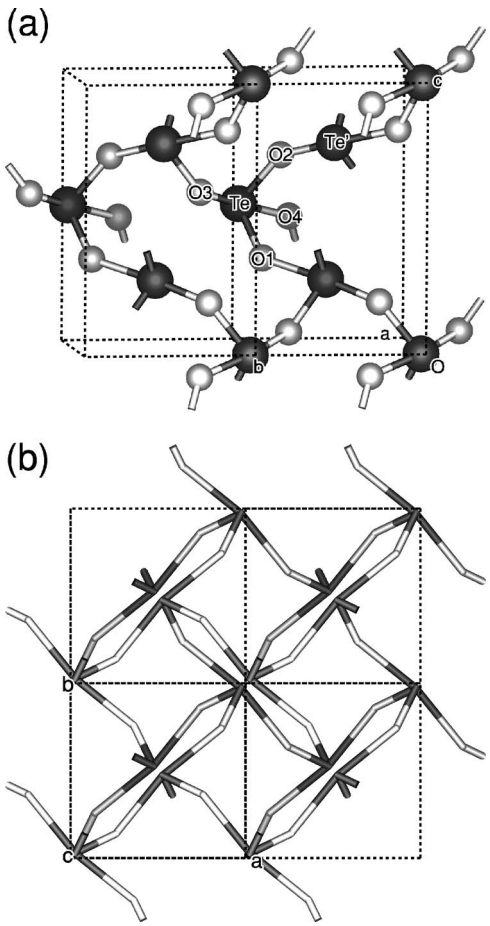

FIG. 2. Structure of α-TeO_2. (a) Perspective view, two unit cells are shown; O2 and O3 (O1 and O4) label the equatorial (axial) oxygen atoms. (b) Four unit cells are drawn along c axis.

TABLE III. Bond lengths and angles for α-TeO_2, calculated with LDA functional, with PBE functional at the theoretical (PBE) and experimental (PBE expt.) lattice parameters, and with BLYP functional at the experimental lattice parameters (BLYP expt.). Experimental x-ray data (Expt.) are from Ref. 4. Atoms are labeled according to Fig. 2.

	LDA	PBE	PBE expt.	BLYP expt.	Expt.
			Bond lengths (Å)		
Te-O1	2.028	1.944	1.954	1.924	1.878
Te-O3	2.170	2.118	2.145	2.134	2.122
Te-Te′	3.855	3.838	3.806	3.779	3.742
			Angles (deg)		
O1-Te-O2	99.8	103.6	103.6	103.7	103.4
O3-Te-O4	161.5	171.2	165.3	166.7	168.0
Te-O2-Te′	135.0	137.1	136.4	137.2	138.6

larger for the LDA than for the PBE functional, but it is sizably reduced by optimizing the internal geometry at the experimental lattice parameters with a marginal improvement for the BLYP functional (cf. Table III). The change in the lattice parameters, bond lengths, and bond angles with volume is reported in Fig. 3. The increase of the c/a ratio with pressure is in agreement with the experimental data of Ref. 24. By increasing the volume, the length of the shorter equatorial bonds decreases while the longer axial bonds increase in length. This behavior would support the picture of α-TeO_2 as made of TeO_2 molecules, inferred from previous lattice dynamics calculations,[8,10,11] which turns out to be in good agreement with our *ab initio* phonon calculations reported in Sec. IV. Although useful for the analysis of the vibrational spectra, the picture of paratellurite as a molecular crystal does not account for all the properties of α-TeO_2. For instance, it can hardly be reconciled with the mostly ionic character and electronic bandwidths of several eV emerging from previous *ab initio* calculations.[21,25]

B. β-TeO_2

The tellurite crystal (space group *Pbca*, D_{2h}^{15}, no. 61) has orthorhombic symmetry with eight formula units per unit cell.[5] Two oxygen and one tellurium atoms are independent by symmetry. The experimental and theoretical (PBE) lattice parameters and positions of the symmetry-independent atoms are given in Table IV. The structural unit of β-TeO_2 is still a TeO_4 trigonal bipyramid, as in α-TeO_2, which forms a network by sharing vertices (bridging oxygen atoms). However, as opposed to paratellurite, the β-TeO_2 crystal has a layered structure with layers oriented perpendicular to the a axis (Fig. 4) and an interlayer distance of $\sim$3 Å.[5] We can still recognize two longer axial bonds and two shorter equatorial bonds, but here all the four Te-O bonds of the TeO_4 unit differ in length. The two-dimensional (2D) network is formed by two- and six-membered Te rings. Still, β-TeO_2 as well can be seen as a molecular crystal made of TeO_2 molecules according to lattice dynamics calculations.[8,10,11]

The calculated independent bond lengths and angles are compared with experimental data in Table V for the PBE functional at the theoretical equilibrium lattice parameters,

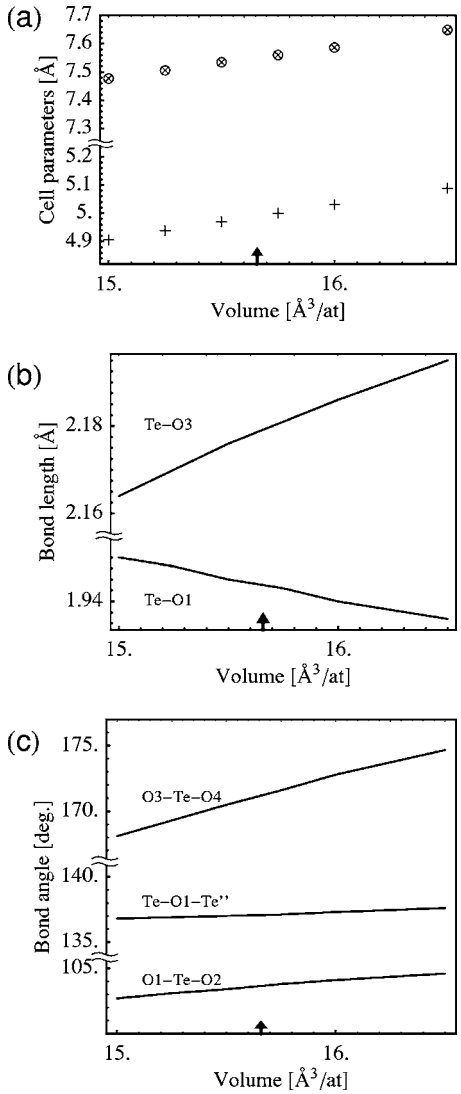

FIG. 3. (a) Lattice parameters (a,c), (b) bond lengths, and (c) bond angles of α-TeO_2 as a function of unit cell volume. The arrow indicates the theoretical equilibrium value. The series in (a) correspond (from bottom to top) to a and c axes. Te-O3 and Te-O1 are the bond lengths of the axial and equatorial bonds, respectively.

TABLE IV. Structural parameters of β-TeO_2, computed using PBE functional at the theoretical (PBE) and experimental (PBE expt.) lattice parameters, and with BLYP functional at the experimental lattice parameters (BLYP expt.). Experimental x-ray data (Expt.) are from Ref. 5.

	PBE	PBE expt.	BLYP expt.	Expt.
		Cell parameters (Å)		
a	12.232			12.035
b	5.523			5.464
c	5.803			5.607
		Atomic positions		
Te *x*	0.1173	0.1193	0.1189	0.1181
Te *y*	0.0263	0.0184	0.0211	0.0252
Te *z*	0.3748	0.3677	0.3682	0.3378
O(1) *x*	0.0314	0.0324	0.0318	0.028
O(1) *y*	0.6491	0.6422	0.6412	0.634
O(1) *z*	0.1613	0.1721	0.1703	0.171
O(2) *x*	0.1714	0.1743	0.1723	0.168
O(2) *y*	0.2174	0.2108	0.2124	0.221
O(2) *z*	0.0812	0.0694	0.0714	0.081

and for PBE and BLYP functionals at the experimental lattice parameters. The same comments on the internal structure presented for α-TeO_2 hold here for β-TeO_2. The spread in the bond lengths of the theoretical geometry at the theoretical lattice parameters (PBE) is reduced with respect to experiments. The misfit is reduced by optimizing the internal geometry at the experimental lattice parameters, with a marginal improvement for the BLYP over the PBE functional. The error in the internal structure thus comes primarily from the overestimation of the equilibrium volume (6%) by the PBE functional. A possible source of error might be the neglect of van der Waals interactions among highly polarizable Te atoms, absent in the LDA and GGA functionals, whose inclusion might bring theoretical and experimental lattice parameters to a closer agreement. The bulk modulus and its derivative with respect to pressure obtained from the fitted Murnaghan equation of state (PBE functional) are $B = 18.4$ GPa ($B = 33$ GPa for α-TeO_2) and $B' = 18.1$. The larger compressibility of β-TeO_2 with respect to α-TeO_2 is due to the weak interlayer interaction, as demonstrated by the evolution of the lattice parameters with volume reported in Fig. 5(a). The *a* axis, perpendicular to the layers, undergoes larger changes with pressure than the other two axes do. However the overestimation of the lattice parameters by the PBE functional is almost the same for all the three axes, which implies that the interlayer interaction should have a strong electrostatic contribution. If the interlayer cohesion were simply given by van der Waals interactions, absent in the GGA functional, the overestimation of the *a* axis by the PBE functional should have been much larger. The change of bond lengths and bond angles with volume is reported in Figs. 5(b) and 5(c). By increasing the volume, the length of the shorter equatorial bonds decreases while the longer axial bonds increase in length. This behavior would support the picture of β-TeO_2 as made of TeO_2 molecules, analogously to α-TeO_2.

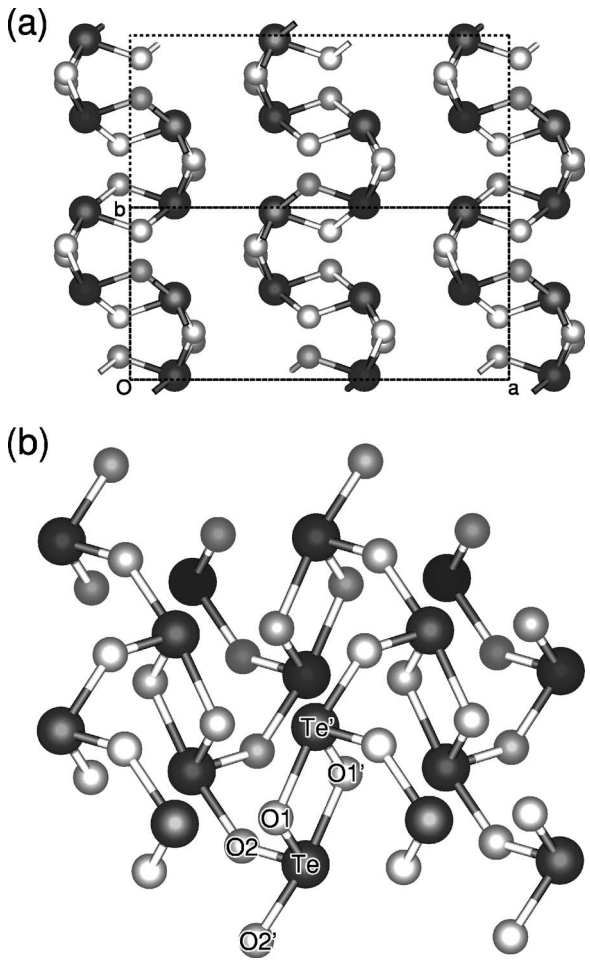

FIG. 4. Layered structure of β-TeO_2. (a) A projection along the *ab* plane. (b) Sketch of a single layer. O1 and O2 (O1′ and O2′) label equatorial (axial) atoms.

C. γ-TeO_2

This phase has been recently identified by recrystallizing amorphous TeO_2 doped with oxides (Nb and W oxides, 10% molar).[6,7] The structure is orthorhombic (space group

TABLE V. Bond lengths and angles for β-TeO_2, using PBE functional at the theoretical (PBE) and experimental (PBE expt.) lattice parameters, and with BLYP functional at the experimental lattice parameters (BLYP expt.). Experimental x-ray data (Expt.) are from Ref. 5. Atoms are labeled according to Fig. 4.

	PBE	PBE expt.	BLYP expt.	Expt.
		Bond lengths (Å)		
Te-O1	1.953	1.960	1.941	1.876
Te-O2	1.968	1.975	1.967	1.893
Te-O1′	2.192	2.186	2.181	2.153
Te-O2′	2.110	2.083	2.067	2.068
Te-Te′	3.232	3.240	3.230	3.168
		Angles (deg)		
O1-Te-O2	97.4	96.8	96.9	98.8
O1′-Te-O2′	169.5	168.9	168.6	165.9
Te-O1-Te′	102.3	102.6	103.0	103.5

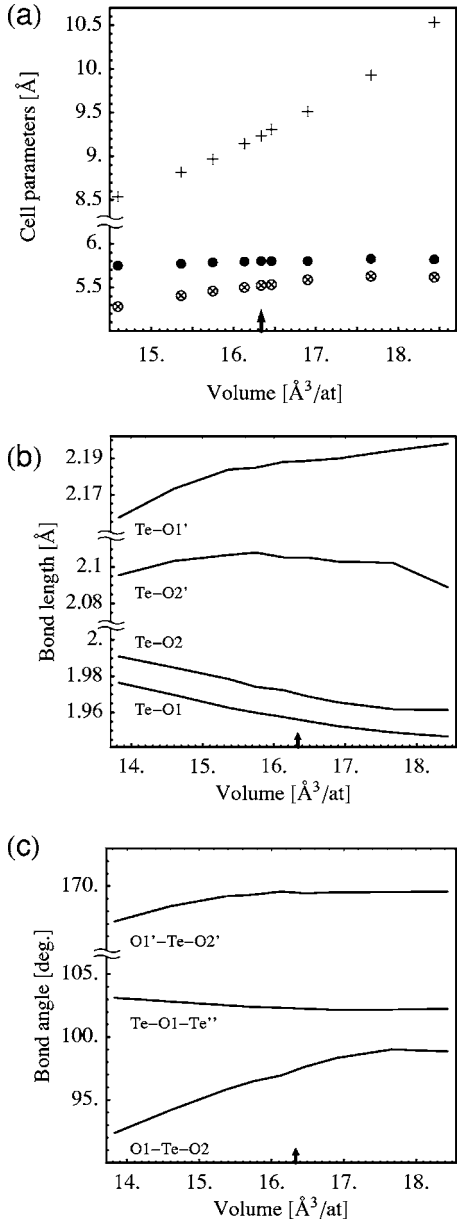

FIG. 5. (a) Lattice parameters (a,b,c), (b) bond lengths, and (c) bond angles of β-TeO_2 as a function of unit cell volume. The arrow indicates the theoretical equilibrium value. The three series in (a) correspond (from bottom to top) to b, c, and a axes. The atom labels refer to Fig. 4. Te-O1 and Te-O2 are equatorial bonds, while Te-O1′ and Te-O2′ are axial bonds.

$P2_12_12_1$, D_2^4, no. 19) with four formula units and three independent atoms per cell. The theoretical (PBE) and experimental lattice parameters and the positions of the independent atoms are reported in Table VI. The error in the theoretical equilibrium volume (11%) and lattice parameters (3%) is slightly larger for γ-TeO_2 than for the other phases. The structure of γ-TeO_2 can still be seen as formed by corner-sharing TeO_4 units with twofold-coordinated oxygen atoms and fourfold-coordinated Te atoms. However, the difference in length of the four Te-O bonds is 0.34 Å, a value sizably larger than in the other phases (0.27 Å for α-TeO_2 and 0.24 Å for β-TeO_2). By considering the longest Te-O bond (2.198 Å) as a nonbonding interaction, γ-TeO_2 would appear as a network of TeO_3 units with Te atoms threefold coordinated, two oxygen atoms twofold coordinated, and one nonbridging onefold-coordinated oxygen atom. The structure of γ-TeO_2 depicted as a fully connected 3D network or as a one-dimensional polymeric structure of TeO_3 units is shown in Figs. 6(a) and 6(b), respectively. The calculated independent bond lengths and angles are compared with experimental data in Table VII for the PBE functional at the theoretical equilibrium lattice parameters and for the PBE and BLYP functionals at the experimental lattice parameters. Still, the spread in the bond lengths is reduced in the theoretical geometry at the theoretical lattice parameters (PBE) with respect to experiments. The larger error in the theoretical lattice parameters shows up in larger errors in the Te-O bond lengths in γ-TeO_2 with respect to the other phases (cf. Tables III and V). The misfit is largely reduced by optimizing the geometry at the experimental lattice parameters, with a marginal improvement for the BLYP over the PBE functional. In particular, the optimized structure at the experimental lattice parameters reproduces the spread of 0.34 Å in the Te-O bond lengths. The change in the lattice parameters, bond lengths, and bond angles with volume is reported in Fig. 7. The shorter Te-O1 bond does not vary with pressure, while both the equatorial Te-O2 bond and the longer Te-O1′ axial bond decrease in length on increasing the volume. Regarding the picture of γ-TeO_2 as a polymeric phase, we note that the longest Te-O bond of the TeO_4 unit (2.198 Å) is only 5% longer than the other axial bond. On the other hand, one notes that in γ-TeO_2 the difference in length between the longer equatorial bond and the short axial bond is the smallest among the three crystalline phases. The polymeric structure would then be seen as generated from the formation of strong intermolecular bonds between the TeO_2 structural units of tellurite and paratellurite rather than from the break-

TABLE VI. Structural parameters of γ-TeO_2, using PBE functional at the theoretical (PBE) and experimental (PBE expt.) lattice parameters, and with BLYP functional at the experimental lattice parameters (BLYP expt.). Experimental x-ray data (Expt.) are from Ref. 7.

	PBE	PBE expt.	BLYP expt.	Expt.
		Cell parameters (Å)		
a	5.176			4.898
b	8.797			8.576
c	4.467			4.351
		Atomic positions		
Te x	0.9581	0.9797	0.9771	0.9696
Te y	0.1032	0.1003	0.1007	0.1016
Te z	0.1184	0.1407	0.1380	0.1358
O(1) x	0.7641	0.7827	0.7801	0.759
O(1) y	0.2851	0.2905	0.2888	0.281
O(1) z	0.1645	0.1853	0.1805	0.173
O(2) x	0.8599	0.8656	0.8646	0.855
O(2) y	0.0406	0.0371	0.0361	0.036
O(2) z	0.7131	0.7237	0.7278	0.727

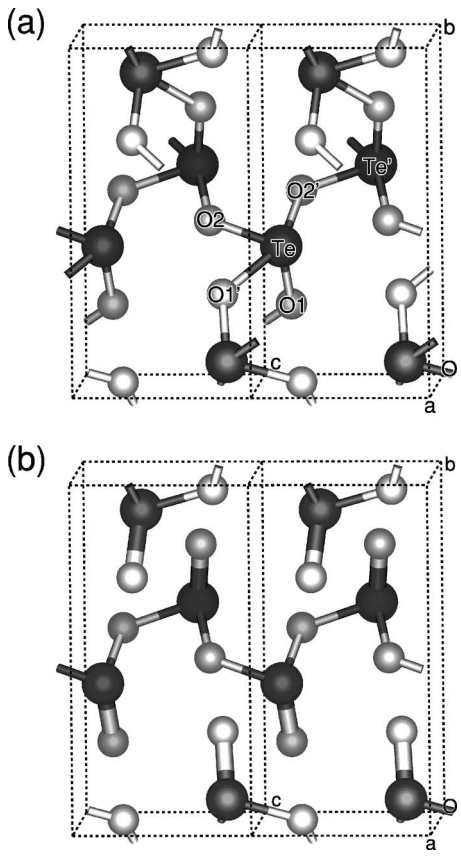

FIG. 6. Structure of γ-TeO_2. Two unit cells are drawn. (a) Three-dimensional structure. (b) Chainlike structure obtained by breaking the longest Te-O bond of the TeO_4 units of (a). O1 and O2 (O1′ and O2′) label equatorial (axial) atoms.

ing of one bond of the TeO_4 units.[6,7,10] The one-dimensional character of γ-TeO_2 has to be supported by the observation of strong anisotropies in the physical properties of this phase. To address this issue, we have calculated the elastic constants of γ-TeO_2 from the difference in the total energy of strained crystals. A maximum strain of 3% has been considered. For

TABLE VII. Bond lengths and angles for γ-TeO_2, using PBE functional at the theoretical (PBE) and experimental (PBE expt.) lattice parameters, and with BLYP functional at the experimental lattice parameters (BLYP expt.). Experimental x-ray data (Expt.) are from Ref. 7. Atoms are labeled according to Fig. 6.

	PBE	PBE expt.	BLYP expt.	Expt.
		Bond lengths (Å)		
Te-O1	1.900	1.905	1.889	1.859
Te-O2	1.960	1.974	1.949	1.949
Te-O1′	2.252	2.257	2.240	2.198
Te-O2′	2.119	2.092	2.081	2.019
Te-Te′	3.596	3.571	3.559	3.521
		Angles (deg)		
O1-Te-O2	99.1	100.7	100.9	101.5
O1′-Te-O2′	156.8	150.9	152.5	153.6
Te-O1-Te′	123.6	122.8	124.0	125.0

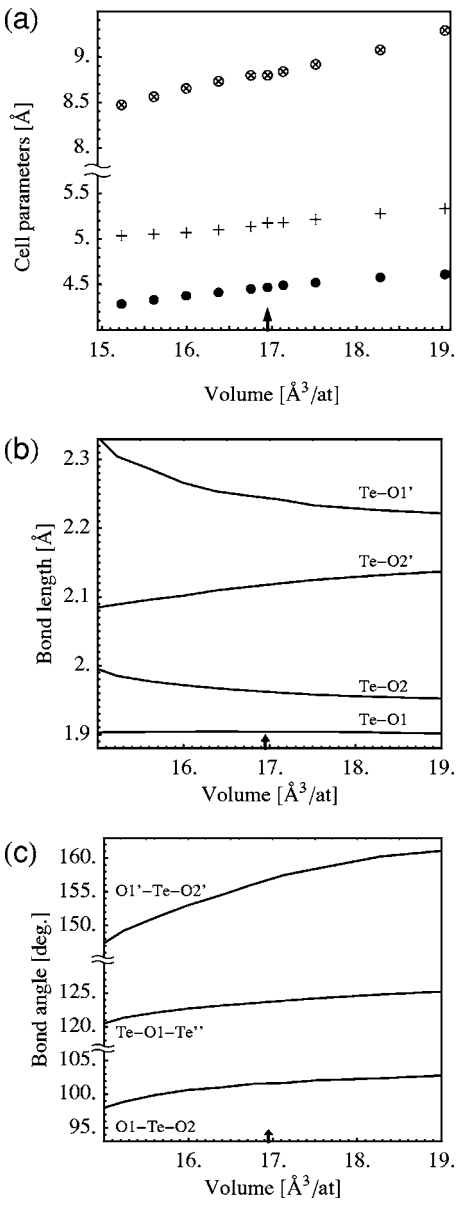

FIG. 7. (a) Lattice parameters (a,b,c), (b) bond lengths, and (c) bond angles of γ-TeO_2 as a function of unit cell volume. The arrow indicates the theoretical equilibrium value. The three series in (a) correspond (from bottom to top) to c, a, and b axes. The atom labels refer to Fig. 6.

stretching along the principal axes we obtain C_{11}=38 GPa, C_{22}=41 GPa, and C_{33}=43 GPa, where the Voigt notation has been used. The bulk modulus and its derivative with respect to pressure obtained from the fitted Murnaghan equation of state (PBE functional) are B=16 GPa (B=33 GPa for α-TeO_2) and B'=6.2. The elastic properties are thus nearly isotropic and do not support the picture of γ-TeO_2 as made of one-dimensional polymeric structure. The elastic constants reported above differ from the results of calculations with empirical interatomic potentials (C_{11}=30 GPa, C_{22}=40 GPa, and C_{33}=67 GPa, Ref. 7), mainly in the C_{33} component which shows an appreciably lower compressibility along the chain (z) axis, not confirmed by our *ab initio* results.

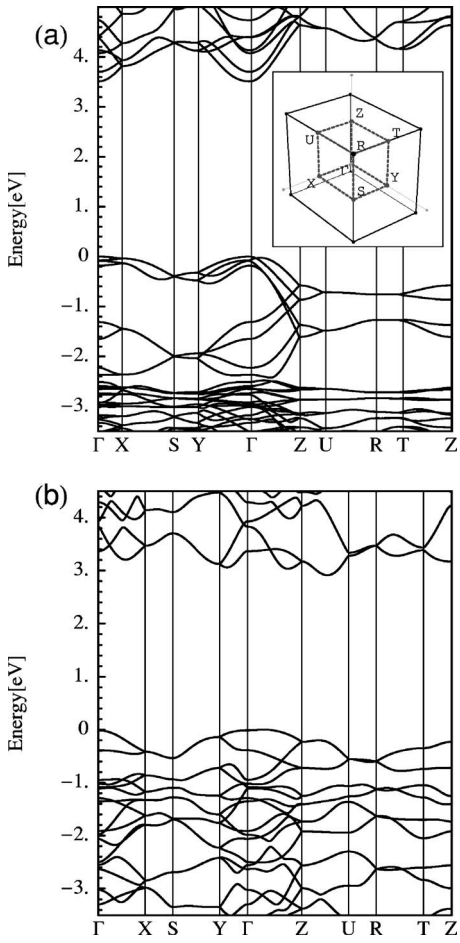

FIG. 8. Electronic band structure of (a) β-TeO_2 and (b) γ-TeO_2. The orthorhombic irreducible Brillouin zone is reported in the inset, equal in shape (but not in size) for both crystals.

We have also contrasted the electronic band structure of γ-TeO_2 and β-TeO_2 phases in Fig. 8. The electronic band structure of α-TeO_2 has been computed within DFT in a previous work.[21] In β-TeO_2, the band dispersion along the direction Γ-X, perpendicular to the 2D layers, is sizably smaller than along the Γ-Y and Γ-Z directions within the layer plane. Conversely, in γ-TeO_2, the dispersion is similar along the three orthogonal directions Γ-X, Γ-Y, Γ-Z. Nor the dispersion along Γ-Z is much larger in γ-TeO_2 than in β-TeO_2, as one would expect by comparing a polymeric phase with chains along z (γ phase) with a mainly molecular crystal made of TeO_2 molecules (β phase). Therefore, the electronic band structure does not provide evidence of a polymeric nature of γ-TeO_2.

We have also computed the formation enthalpy and formation free energy at normal conditions (298.15 K, $p=1$ bar) for the three crystalline phases, by including the phononic contribution to the free energy and enthalpy. Only Γ-point phonons have been included in the calculation (see Sec. IV). For α-TeO_2 we have verified that the phononic contribution to the free energy of −7.8 kJ/mol, which includes only Γ-point phonons, changes to −6.7 kJ/mol by including in the calculation the full phonon density of states. Formation free energies and enthalpies have been computed with PBE functionals at the theoretical equilibrium structure for all three phases.

The calculated formation enthalpy (ΔH_f) and free energy (ΔG_f) of α-TeO_2, with respect to crystalline Te and gaseous O_2 (the standard states), are $\Delta H_f = -287.5$ kJ/mol (expt. −322.6 kJ/mol),[22] and $\Delta G_f = -232.8$ kJ/mol (expt. −270.3 kJ/mol).[22] The error is within the usual accuracy of DFT methods. The free energies of gaseous Te_2 and O_2 have been calculated from the molecule optimized in the triplet state,[23] by including translational, vibrational, and rotational contributions. The free energy of crystalline Te has been computed from theoretical and experimental[22] free energies of the gaseous Te_2 molecule.

For β-TeO_2 the calculated formation enthalpy and free energy are $\Delta H_f = -289.3$ kJ/mol and $\Delta G_f = -236.3$ kJ/mol, while for γ-TeO_2 $\Delta H_f = -284.6$ kJ/mol and $\Delta G_f = -229.8$ kJ/mol. To our knowledge, no experimental data on formation energies are available for β-TeO_2 and γ-TeO_2.

IV. VIBRATIONAL PROPERTIES

Phonons at the Γ point have been calculated within density functional perturbation theory.[18] The modes that display a dipole moment couple to the inner macroscopic longitudinal electric field which shifts the LO phonon frequencies via the nonanalytic contribution to the dynamical matrix[18]

$$D^{NA}_{\alpha\beta}(\kappa,\kappa') = \frac{4\pi}{V_o}\frac{Z_{\alpha\alpha'}(\kappa)q_{\alpha'}Z_{\beta\beta'}(\kappa')q_{\beta'}}{\mathbf{q}\cdot\underline{\underline{\epsilon}}^{\infty}\cdot\mathbf{q}}, \tag{1}$$

where $\underline{\underline{Z}}$ and $\underline{\underline{\epsilon}}^{\infty}$ are the effective charges and electronic dielectric tensors, V_o is the unit cell volume, and $\mathbf{q}$ is the phononic wave vector. The macroscopic field contribution to the dynamical matrix [Eq. (1)] introduces an angular dispersion of the phonons at the Γ point, i.e., the limit of the phononic bands $\omega(\mathbf{q})$ for $\mathbf{q}\to\mathbf{0}$ depends on the angles formed by $\mathbf{q}$ with the principal axes. For a uniaxial crystal like α-TeO_2, the phonon frequencies depend on the angle θ formed by $\mathbf{q}$ with the optical axis. For the orthorhombic crystals β-TeO_2 and γ-TeO_2, the phonon frequencies depend on the polar angles θ and ϕ which define the orientation of $\mathbf{q}$ with respect to the crystallographic axes, coinciding with the optical principal axes.

The dielectric tensor is given in terms of phonons and effective charges by

$$\epsilon_{\alpha\beta}(\omega) = \epsilon^{\infty}_{\alpha\beta} + \frac{4\pi}{V_o}\sum_{j=1}^{3N} p_\alpha(j)p_\beta(j)\frac{1}{\omega_j^2-\omega^2} \tag{2}$$

where $\mathbf{p}(j)$ is given by

$$p_\alpha(j) = \sum_{\kappa=1}^{N} Z_{\alpha\beta}(\kappa)\frac{e_\beta(j,\kappa)}{\sqrt{M_\kappa}}. \tag{3}$$

The sum over κ runs over the N atoms in the unit cell with mass M_κ. $e(j,\kappa)$ and ω_j are the eigenstates and eigenvalues of the dynamical matrix at the Γ point, without the contribution of the macroscopic field. The absorption coefficient α_γ for light polarized along the crystallographic axis γ is

$$\alpha_\gamma(\omega) = \frac{\omega}{nc}\,\mathrm{Im}\,\epsilon_{\gamma\gamma}(\omega + i\eta, \eta \to 0) = \frac{2\pi^2}{V_o nc}\sum_j |p_\gamma(j)|^2 \delta(\omega - \omega_j) = \frac{\pi}{2nc}\sum_j f_j \omega_j^2 \delta(\omega - \omega_j), \quad (4)$$

where c is the velocity of light in vacuum and $n(\omega)$ is the (frequency-dependent) real part of the refractive index.

In order to compare the theoretical results with available experimental data we have also computed the IR absorption for a polycrystalline sample. This amounts to averaging the absorption coefficient for the two polarizations of the electromagnetic wave (ordinary and extraordinary waves for uniaxial crystals, for instance) over the solid angle of the possible wave vectors $\mathbf{q}$ of the transmitted wave. The absorption coefficient for a generic $\mathbf{q}$ is obtained by solving the Fresnel equations for the dielectric tensor defined by Eq. (2).[26]

The differential cross section for Raman scattering (Stokes) in nonresonant conditions is given by the following expression (for a unit volume of scattering sample):

$$\frac{d^2\sigma}{d\Omega\, d\omega} = \sum_j \frac{\omega_S^4}{c^4} |\mathbf{e}_S \cdot \underline{\underline{R}}^j \cdot \mathbf{e}_L|^2 [n_B(\omega) + 1] \delta(\omega - \omega_j), \quad (5)$$

where $n_B(\omega)$ is the Bose factor, ω_S is the frequency of the scattered light, and $\mathbf{e}_S$ and $\mathbf{e}_L$ are the polarization vectors of the scattered and incident light, respectively.[27,28] The Raman tensor $\underline{\underline{R}}^j$ associated with the jth phonon is given by

$$R^j_{\alpha\beta} = \sqrt{\frac{V_o \hbar}{2\omega_j}} \sum_{\kappa=1}^{N} \frac{\partial \chi^\infty_{\alpha\beta}}{\partial \mathbf{r}(\kappa)} \cdot \frac{\mathbf{e}(j,\kappa)}{\sqrt{M_\kappa}}, \quad (6)$$

where V_o is the unit cell volume, $\mathbf{r}(\kappa)$ is the position of the κth atom, and $\underline{\underline{\chi}}^\infty = (\underline{\underline{\epsilon}}^\infty - 1)/4\pi$ is the electronic susceptibility. The tensor $\underline{\underline{R}}^j$ is computed from $\underline{\underline{\chi}}^\infty$ by finite differences, by moving the atoms independent by symmetry with maximum displacement of 0.01 Å.

Whenever the experimental Raman spectrum is available only for a polycrystalline sample, Eq. (5) must be integrated over the solid angle in order to compare the theoretical spectra with experiments. In particular, the Raman spectrum for nonpolarized light is obtained by summing over all possible polarization vectors $\mathbf{e}_S$ and $\mathbf{e}_L$ consistent with the scattering geometry. In the case of β-TeO_2, the inner longitudinal macroscopic field has no effect on the Raman active modes due to the presence of an inversion symmetry. In fact, the Raman-active g modes have no dipole moment to couple with the macroscopic longitudinal field. As a consequence for β-TeO_2 there is no angular dispersion for the Raman-active modes and the total cross section for unpolarized light in backscattering geometry is obtained from Eq. (5) with the substitution

$$4(R_{xx}^2 + R_{yy}^2 + R_{zz}^2) + 7(R_{xy}^2 + R_{xz}^2 + R_{yz}^2) + (R_{xx}R_{yy} + R_{xx}R_{zz} + R_{zz}R_{yy}) \to 30|\mathbf{e}_S \cdot \underline{\underline{R}}^j \cdot \mathbf{e}_L|^2. \quad (7)$$

Conversely, for α-TeO_2 and γ-TeO_2 the presence of angular dispersion requires the integral over the solid angle to be performed by summing over discrete points in the polar angles. Phonon frequencies and eigenvectors entering in Eqs. (5) and (6) are modified by the macroscopic longitudinal field along the direction assigned by the crystal momentum transferred in the scattering process.

The δ functions in Eqs. (4) and (5) are approximated by Lorentzian functions as

$$\delta(\omega - \omega_j) = \frac{4}{\pi} \frac{\omega^2 \Delta\omega_j}{(\omega^2 - \omega_j^2)^2 + 4\Delta\omega_j^2 \omega^2} \quad (8)$$

with $\Delta\omega_j$ half-linewidth fitted on the experimental Raman peaks when available and otherwise assigned to a constant value of 4 cm^{-1} (cf. Table VIII).

A. α-TeO_2

Phonons at the Γ point can be classified according to the irreducible representations of the D_4 point group of α-TeO_2 as $\Gamma = 4A_1 + 4A_2 + 5B_1 + 4B_2 + 8E$, where the acoustic modes (A_2 and E) have been omitted. The A_1, B_1, B_2, and E modes are Raman active, while the A_2 and E modes are IR active. The calculated phonon frequencies at the Γ point neglecting the contribution of the macroscopic longitudinal field are given in Table VIII for the BLYP calculation at the experimental lattice parameters. The angular dispersion of A_2 and E modes due to the macroscopic electric field is reported in Fig. 9; it is in good agreement with the angular dispersion obtained experimentally from the IR absorption peaks of the extraordinary waves (cf. Fig. 3 of Ref. 29). Experimental frequencies and IR activities of IR-active modes [A_2 and E(TO) modes] are also reported in Table VIII. Experimental frequencies from Raman spectra are also reported in Table VIII for A_1, B_1, and B_2 modes. For Raman-active E(LO) modes the comparison is made directly between the theoretical and experimental Raman spectra, since their frequencies depend on the scattering geometries. Phonon frequencies calculated with the PBE or LDA functional at the theoretical lattice parameters and with PBE and BLYP functionals at the experimental lattice parameters are compared in Table VIII. The best agreement with experiments is obtained for BLYP calculations at the experimental lattice parameters which give the equilibrium internal geometry closest to the experimental structure (cf. Sec. III A). The IR oscillator strengths are in good agreement with experiments, apart from the overestimation of the intensity of mode $A_2(2)$. Experimental data from a more recent work[30] are very similar (within 5 cm^{-1}) to the older experimental data reported in Table VIII, but for the oscillator strength (f) of mode $A_2(2)$ which is 3.33 in Ref. 30, in closer agreement with our theoretical result. The IR absorption spectrum for a polycrystalline sample, computed as described in the previous section is reported in Fig. 10; it has to be compared with the experimental spectrum reported in Fig. 2 of Ref. 8. The linewidth of the phononic modes is chosen according to the IR experimental data on single crystal.[29] The two broad bands and the shoulder at

TABLE VIII. Theoretical phonon frequencies of α-TeO_2 at the Γ point, oscillator strengths [f_j in Eq. (4)] of IR-active modes and squared coefficients of the Raman tensor of the Raman-active modes, a^2 and b^2 for A_1, c^2 for B_1, d^2 for B_2, and e^2 for E_x, E_y modes (in units of 10^{-3} Å^3; see Sec. IV). The contribution of the inner longitudinal macroscopic field is not included (LO-TO splitting). All the theoretical values correspond to calculations with the BLYP functional at the experimental lattice parameters. Experimental data on phonon frequencies and oscillator strengths from IR absorption spectra at 85 K (Ref. 29) are given in parentheses for (TO) A_2 and E modes. Experimental phonon frequencies of A_1, B_1, and B_2 modes (in parentheses) are taken from Raman spectra at 85 K (Ref. 33). $\Delta\omega$ indicate the phonon half-linewidths obtained by fitting the main peaks of the polycrystalline Raman spectra at 295 K (cf. Fig. 13).

Mode	ω (cm^{-1})	f_j	a^2 (c^2, d^2, e^2)	b^2	$\Delta\omega$
B_1 (1)	42 (62)		2.044		
A_2 (1)	90 (76)	7.758 (12.95)			
E (1)	124 (124)	0.919 (1.28)	5.158		2.9
B_1 (2)	128		0.042		
A_1 (1)	143 (152)		4.939	7.561	5.8
B_2 (1)	148 (157)		2.767		2.2
B_1 (3)	175 (179)		0.324		
E (2)	175 (177)	5.667 (8.05)	0.980		
E(3)	212 (212)	3.127 (2.02)	0.043		
A_1 (2)	214 (218)		0.338	0.058	
B_1 (4)	229 (235)		0.514		
A_2 (2)	269 (265)	3.156 (0.77)			
B_2 (2)	272 (281)		0.330		
E (4)	291 (299)	5.121 (3.95)	0.045		
A_2 (3)	302 (325)	4.096 (4.70)			
E (5)	325 (336)	0.005 (0.25)	0.077		
E (6)	336 (379)	0.006 (0.01)	0.863		6.4
A_1 (3)	383 (391)		2.421	7.923	12.1
B_2 (3)	406 (415)		0.136		
A_2 (4)	535 (570)	3.802 (3.86)			
B_1 (5)	537 (589)		1.551		14.0
E (7)	594 (644)	1.268 (1.27)	0.200		
A_1 (4)	598 (649)		10.242	14.815	4.7
E (8)	700 (774)	0.225 (0.21)	0.671		
B_2 (4)	726 (786)		0.574		

lower frequency in the experimental spectrum[8] are well reproduced, but for the already mentioned redshift in the theoretical frequencies.

The Raman tensor [Eq. (6)] for the Raman-active irreducible representations has the following form:[31]

$$A_1 \Rightarrow \begin{bmatrix} a & . & . \\ . & a & . \\ . & . & b \end{bmatrix}, \quad B_1 \Rightarrow \begin{bmatrix} c & . & . \\ . & -c & . \\ . & . & . \end{bmatrix},$$

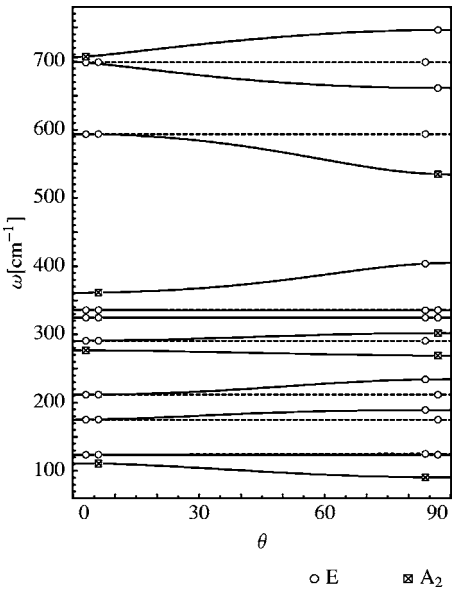

FIG. 9. Angular dispersion of E and A_2 IR-active modes in α-TeO_2. Dashed lines represent unshifted (i.e., TO) E modes.

$$B_2 \Rightarrow \begin{bmatrix} . & d & . \\ d & . & . \\ . & . & . \end{bmatrix}, \quad E_x(y) \Rightarrow \begin{bmatrix} . & . & (-e) \\ . & . & e \\ (-e) & e & . \end{bmatrix}.$$

The coefficients a, b, c, d, and e calculated from first principles as outlined above are given for each mode in Table VIII. The calculated derivatives of the dielectric tensor with respect to the displacement of the atoms independent by symmetry are given as additional material.[32]

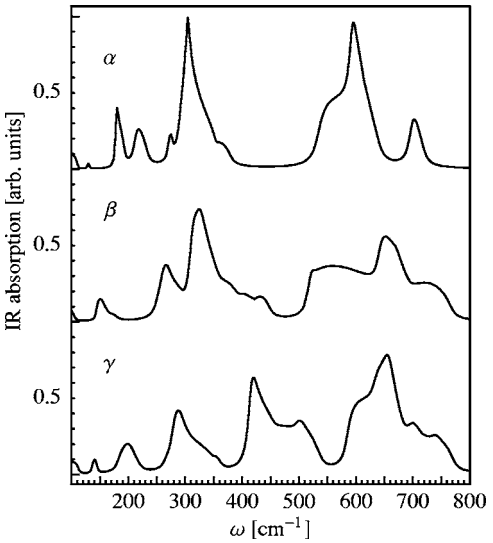

FIG. 10. IR absorption [$\alpha(\omega)$, cf. Eq. (4)] spectra for polycrystalline samples of α-, β-, and γ-TeO_2; linewidths in α-TeO_2 are taken from experimental data on single crystals (Ref. 29). In the absence of experimental data, the linewidths of β- and γ-TeO_2 are chosen analogously to those of the α phase, i.e., 5 cm^{-1} for modes with frequency lower than 150 cm^{-1}, and 15 cm^{-1} for higher-frequency modes.

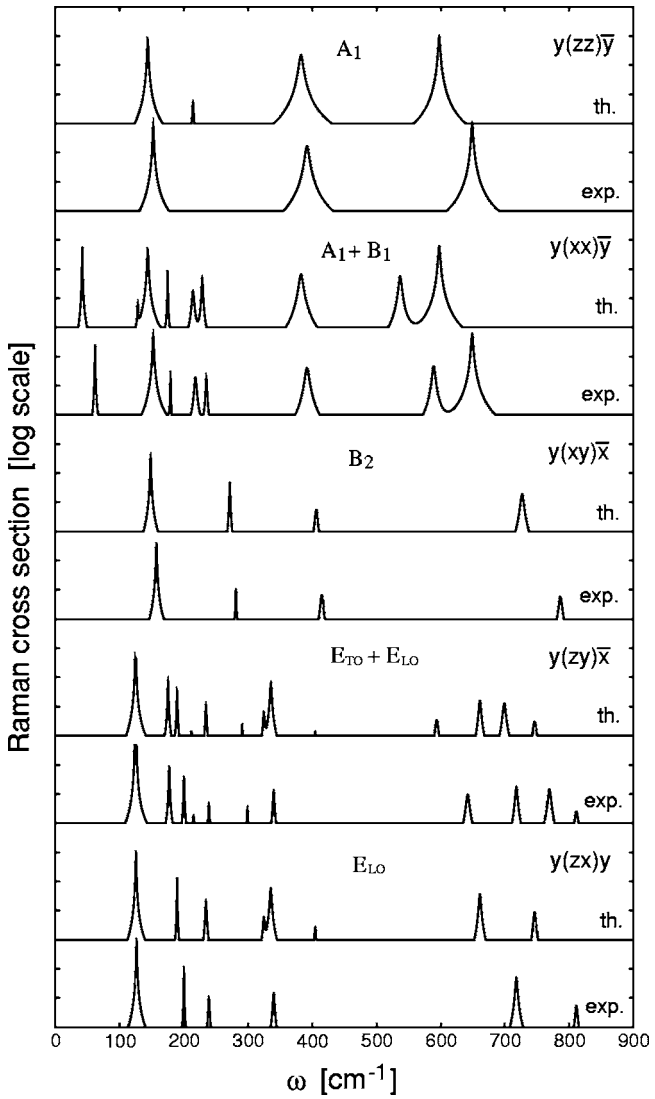

FIG. 11. Raman spectra of α-TeO_2 single crystal for different scattering geometries. Theoretical spectra (th.) are computed with the BLYP functional at experimental lattice parameters. The experimental spectra at 85 K are adapted from Ref. 33. The character of the modes active in each scattering geometry is also reported. The linewidths of the theoretical peaks are fitted on the experimental spectra whenever the correspondence is unambiguous. The Raman intensities are reported on a logarithmic scale for sake of comparison with the experimental data of Ref. 33. The experimental peak is normalized to the strongest peak of the corresponding theoretical spectrum.

The theoretical Raman spectra for different scattering conditions, each selecting particular modes, are compared with experimental data[7,33] in Fig. 11. The theoretical spectra include the shift in phonon frequencies due to the contribution of the macroscopic longitudinal field along the direction assigned by the crystal momentum transferred in the scattering geometry. The Raman spectrum for a polycrystalline sample is also computed and compared with experimental data in Fig. 13 below. For each wave vector **q** transferred in the scattering process the phonon eigenvector and frequency are computed by including the nonanalytic part of the dynamical matrix. The solid angle average is performed over 256 angles independent by symmetry. The linewidth of the most intense Raman peaks in the theoretical spectra has been obtained by fitting the experimental spectra with a sum of Lorentzian functions, either at 85 K for the single-crystal spectra (Fig. 11) or at 295 K for the polycrystalline spectra. The high-temperature half-linewidths are given in Table VIII. The half-linewidth of the weaker or less identifiable peaks is set to 4 cm^{-1}.

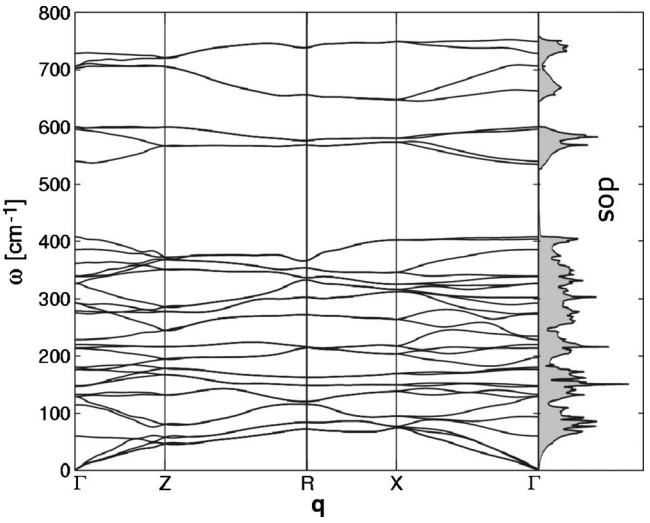

FIG. 12. Phonon dispersion relations and density of states of α-TeO_2, calculated with BLYP functional at the experimental lattice parameters.

The calculated Raman spectra are in good agreement with experiments on peak intensities and also on peak frequencies in the low-frequency region, while the high-frequency modes appear too soft by nearly 8% (see Table VIII). The discrepancy can possibly be ascribed to the partial homogenization of axial and equatorial bonds resulting from the use of approximate exchange-correlation functionals. This effect is smaller for the BLYP than for the PBE functionals (cf. Sec. III A). The experimental Raman peak at 218 cm^{-1} assigned to a B_1 mode in Ref. 33 can be better assigned to the $A_1(2)$ mode on the base of our calculations (cf. Table VIII) which is also not inconsistent with experimental two-phonon IR spectra of Ref. 30. More on the displacement pattern of the different modes is given in Sec. IV D where the Raman spectra of the three phases are compared.

Phonon dispersion relations along the high-symmetry directions of the irreducible Brillouin zone (IBZ) and phonon density of states (DOS) are reported in Fig. 12. The dynamical matrices have been computed for 30 **q** points along the Γ-*Z*-*R*-*X*-Γ path shown in Fig. 12, or on a $4\times4\times4$ grid in **q** space for the DOS calculation. A Fourier interpolation technique provided the dynamical matrix at the other points of the BZ.[18] For the DOS calculation, we have used the tetrahedron method on a mesh of $20\times20\times20$ points in the IBZ.

An energy gap separates the low-frequency phonon branches from the eight highest-frequency bands, which can be assigned to stretching modes of the eight inequivalent Te-O bonds per cell, i.e., symmetric and antisymmetric stretching modes of the four TeO_2 in the unit cell (see Sec.

IV D). This group of bands is slightly shifted downward with respect to experiments, as discussed above. Our results compare fairly well with previous lattice dynamics calculations of the DOS (Refs. 8 and 11) and on dispersion relations.[9] However, sizable quantitative differences are present especially on angular dispersion with respect to shell model calculations.[9] To our knowledge, no experimental data are available on phonon dispersion relations.

B. β-TeO_2

Phonons at the Γ point can be classified according to the irreducible representations of the D_{2h} point group as $\Gamma = 9(A_g + A_u + B_{1g} + B_{2g} + B_{3g}) + 8(B_{1u} + B_{2u} + B_{3u})$. The three translation modes have been omitted. The g modes are Raman active while B_u modes are IR active. Only B_u modes couple to the macroscopic longitudinal field via the nonanalytic part of the dynamical matrix. The calculated phonon frequencies at the Γ point, neglecting the contribution of the longitudinal macroscopic field, are given in Table X. The results refer to calculations at the experimental lattice parameters with the BLYP functional, which turned out to provide the best agreement with experiments for α-TeO_2 and for β-TeO_2 as well.

The Raman tensor for the active modes of an orthorhombic crystal has the form[31]

$$A \Rightarrow \begin{bmatrix} a & . & . \\ . & b & . \\ . & . & c \end{bmatrix}, \quad B_1(z) \Rightarrow \begin{bmatrix} . & d & . \\ d & . & . \\ . & . & . \end{bmatrix},$$

$$B_2(y) \Rightarrow \begin{bmatrix} . & . & e \\ . & . & . \\ e & . & . \end{bmatrix}, \quad B_3(x) \Rightarrow \begin{bmatrix} . & . & . \\ . & . & f \\ . & f & . \end{bmatrix}.$$

For β-TeO_2 only the g modes have to be considered.

The calculated coefficients of the Raman tensor are given in Table X for all active modes. Experimental Raman spectra are available only for polycrystalline samples in backscattering geometry for unpolarized light.[7] The corresponding theoretical spectrum can be obtained by averaging the Raman cross section over the solid angle by making use of Eq. (7). The resulting theoretical Raman spectrum of β-TeO_2 is compared with the experimental powder spectrum in Fig. 13. The linewidth of the most intense Raman peaks in the theoretical spectra has been obtained by fitting the experimental spectra with a sum of Lorentzian functions. The results are given in Table X. The half-linewidth of the weaker or less identifiable peaks is set to 4 cm^{-1}. Overall the experimental spectrum is well reproduced, but for a redshift of the high-frequency modes. The underestimation of the frequency of the stretching modes is probably due to the overestimation of the Te-O bond length (cf. Sec. III B). The frequency redshift with respect to experiments is even larger when the PBE functional is used, as occurs for the α-TeO_2 (cf. Table IX). The theoretical Raman spectrum allows us to assign the character of the modes responsible for the experimental

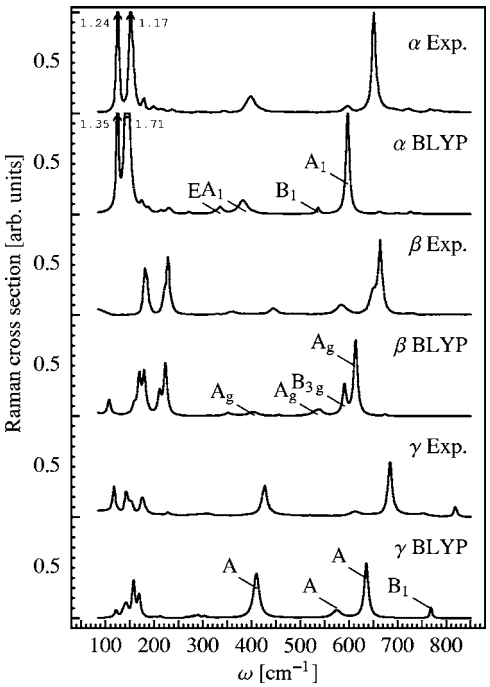

FIG. 13. Unpolarized Raman spectra of polycrystalline α-, β-, and γ-TeO_2 for backscattering geometry. Theoretical spectra are calculated with the BLYP functional at the experimental lattice parameters. Experimental spectra are also shown for comparison (Ref. 7). For each phase the experimental spectrum is normalized over the strongest high-frequency peak of the theoretical spectrum.

peaks. More on the displacement pattern of the different modes is given in Sec. IV D where the Raman spectra of the three phases are compared.

The B_u modes are subject to angular dispersion due to the coupling with the macroscopic longitudinal field. The dependence of the phonon frequencies on the polar angles of the **q** vector approaching the Γ point is given in Fig. 14. The IR oscillator strength of the active modes is reported in Table X. To our knowledge no experimental IR data are available for single crystals. To compare with experimental data available we have thus computed the IR absorption spectrum for a polycrystalline sample as described in the previous section. The result is reported in Fig. 10; it has to be compared with the experimental spectrum reported in Fig. 2 of Ref. 8. The experimental peaks are reproduced qualitatively, but for an inversion in the relative intensities of the two peaks around 600 and 700 cm^{-1}. Moreover, the theoretical spectrum shows a shoulder at high frequency which is absent in the experimental spectrum. Our choice of the phonon linewidth might be partially responsible for these disagreements with the experimental data. In fact, in the absence of experimental data, the linewidth of the phononic modes is chosen similarly to those of α-TeO_2, i.e., 5 cm^{-1} for frequency below 150 cm^{-1} and 15 cm^{-1} for higher frequencies.

C. γ-TeO_2

Phonons at the Γ point can be classified according to the irreducible representations of the D_2 point group as Γ

TABLE IX. Phonon frequencies (cm^{-1}) of α-TeO_2 computed with BLYP functional at the experimental lattice parameters (BLYP expt.), with PBE and LDA functionals at the theoretical lattice parameters and with PBE at the experimental lattice parameters (PBE expt.).

Mode	BLYP expt.	PBE expt.	PBE	LDA
$B_1(1)$	42	48	62	69
$A_2(1)$	90	94	90	106
$E(1)$	124	120	116	142
$B_1(2)$	128	127	125	129
$A_1(1)$	143	140	134	135
$B_2(1)$	148	141	136	131
$B_1(3)$	175	171	150	166
$E(2)$	175	171	162	179
$E(3)$	212	214	193	213
$A_1(2)$	214	207	195	206
$B_1(4)$	229	234	218	251
$A_2(2)$	269	267	254	256
$B_2(2)$	272	261	235	241
$E(4)$	291	282	262	262
$A_2(3)$	302	292	286	284
$E(5)$	325	316	295	327
$E(6)$	336	335	317	334
$A_1(3)$	383	377	364	402
$B_2(3)$	406	399	385	404
$A_2(4)$	535	507	515	471
$B_1(5)$	537	512	509	484
$E(7)$	594	573	567	551
$A_1(4)$	598	579	575	555
$E(8)$	700	683	694	667
$B_2(4)$	726	701	706	667

$=8(B_1+B_2+B_3)+9A$. The three translational modes have been omitted. The calculated phonon frequencies at the Γ point, neglecting the contribution of the longitudinal macroscopic field is given in Table XI. The results refer to calculations at the experimental lattice parameters with the BLYP functional. All the modes are Raman active while only B modes are IR active and display angular dispersion due to the coupling with the longitudinal macroscopic field (Fig. 15). The IR oscillator strength of the active modes is reported in Table XI. Still no experimental IR data are available for γ-TeO_2 single crystals. To compare with experimental data available we have thus computed the IR absorption spectrum for a polycrystalline sample as described in the previous section. The result is reported in Fig. 10; it has to be compared with the experimental spectrum reported in Fig. 2 of Ref. 8. In the absence of experimental data, the linewidth of the phononic modes is chosen similarly as 5 cm^{-1} for frequency below 150 cm^{-1} and 15 cm^{-1} for higher frequencies, analogously to α-TeO_2. The theoretical spectrum reproduces all the main features of the experimental spectrum,[8] but for a redshift of the theoretical modes at high frequency as occurs for α-TeO_2.

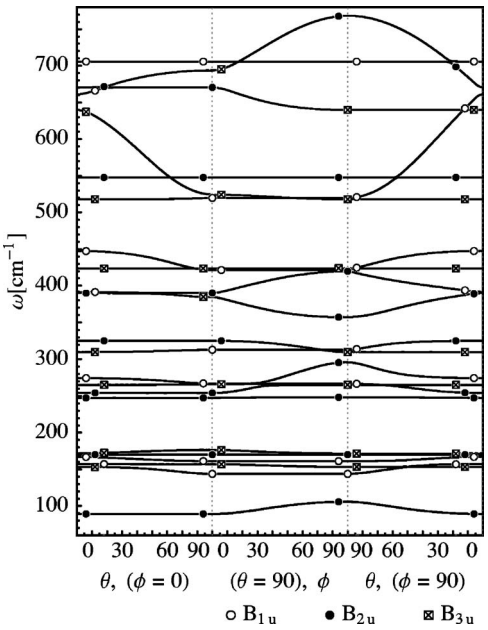

FIG. 14. Angular dispersion of IR-active modes in β-TeO_2.

The Raman tensor for active modes has been given in the previous section. The coefficients of the theoretical Raman tensor are given in Table XI for all the active modes. As for β-TeO_2, experimental Raman spectra are available only for polycrystalline samples in backscattering geometry. The corresponding theoretical spectrum can be obtained by averaging the Raman cross section over the solid angle. However, as opposed to the case of β-TeO_2, Raman-active modes in γ-TeO_2 can be subject to angular dispersion (cf. Fig. 15). As a consequence the formula in Eq. (7) cannot be used and the integral over the solid angle has to be performed over discrete angular values of the phononic wave vector $\mathbf{q}$ approaching the Γ point. For each wave vector $\mathbf{q}$ transferred in the scattering process the phonon eigenvector and frequency are computed by including the nonanalytic part of the dynamical matrix. The solid angle average is performed over 256 angles independent by symmetry. The calculated powder Raman spectrum of γ-TeO_2 is compared with the experimental spectra and with the spectra of the other phases in Fig. 13. The linewidths of the theoretical peaks are fitted to experiments as discussed for β-TeO_2 in the previous section. The half-linewidth of the weaker or less identifiable peaks is set to 4 cm^{-1}. The half-linewidths of the Raman-active modes are reported in Table XI. The angular dispersion has a minor effect on the Raman spectrum since the most intense peaks turn out to have A character for which no coupling exists with the longitudinal macroscopic field: the Raman powder spectra of γ-TeO_2 including or neglecting the angular dispersion are indistinguishable on the scale of Fig. 13. The agreement between theory and experiments is overall good as for the other phases. Still, a sizable redshift of the high-frequency modes is present. Analogously to the other phases, the error is still slightly larger by making use of the PBE functional. Moreover, a very weak experimental peak around 790 cm^{-1} has no counterpart in the calculated spectrum. Although three Raman-active modes fall in that region, none of

TABLE X. Theoretical phonon frequencies of β-TeO_2 at the Γ point, oscillator strengths [f_j in Eq. (4)] of IR-active modes and squared coefficients of the Raman tensor of the Raman-active modes (in units of 10^{-3} Å^3; see Sec. IV). The contribution of the inner longitudinal macroscopic field is not included (LO-TO splitting). All the theoretical values correspond to calculations with the BLYP functional at the experimental lattice parameters. The phonon half-linewidths ($\Delta\omega$) are obtained by fitting the experimental Raman spectra of a polycrystalline sample (Ref. 7) with a sum of Lorentzian functions (Fig. 13).

Mode	ω (cm^{-1})	f_j	a^2 (d^2)	b^2 (e^2)	c^2 (f^2)	$\Delta\omega$
$A_u(1)$	38					
$B_{3u}(1)$	44	0.049				
$B_{1u}(1)$	55	0.092				
$B_{3g}(1)$	56				3.828	
$A_g(1)$	67		0.576	1.607	2.645	
$B_{1g}(1)$	72		0.000			
$B_{2g}(1)$	77			0.310		
$A_u(2)$	85					
$B_{2u}(1)$	89	5.487				
$A_g(2)$	108		0.542	3.133	1.998	
$B_{2g}(2)$	123			0.186		
$B_{1u}(2)$	144	5.503				
$B_{3u}(2)$	153	0.586				
$B_{1g}(2)$	159		0.612			
$B_{1u}(3)$	161	0.398				
$A_u(3)$	163					
$B_{3g}(2)$	169				2.952	3.5
$B_{2u}(2)$	170	0.015				
$B_{3u}(3)$	171	0.478				
$A_g(3)$	180		1.157	2.548	1.650	3.2
$B_{2g}(3)$	188			0.324		
$B_{3g}(3)$	208				0.044	
$B_{1g}(3)$	209		0.003			
$A_g(4)$	211		1.163	3.532	2.730	3.4
$B_{2g}(4)$	212			0.257		
$B_{2g}(5)$	222			0.049		
$A_g(5)$	223		7.267	0.819	1.616	4.4
$B_{1g}(4)$	231		0.138			
$B_{3g}(4)$	234				0.001	
$A_u(4)$	235					
$B_{2u}(3)$	247	0.666				
$B_{2u}(4)$	254	3.949				
$A_u(5)$	258					
$B_{3u}(4)$	265	0.094				
$B_{1u}(4)$	267	2.050				
$B_{3u}(5)$	310	2.893				
$B_{1g}(5)$	312		0.171			
$B_{1u}(5)$	313	6.503				
$B_{3g}(5)$	317				0.002	
$B_{2u}(5)$	325	0.940				
$A_u(6)$	336					
$B_{3g}(6)$	349				0.000	
$B_{1g}(6)$	352		0.400			
$A_g(6)$	354		2.525	0.078	0.120	
$A_u(7)$	377					
$B_{2u}(6)$	390	0.455				
$B_{2g}(6)$	397			0.127		
$A_g(7)$	404		0.112	1.411	4.031	13.4
$B_{2g}(7)$	408			0.129		
$B_{1u}(6)$	421	0.590				
$B_{3u}(6)$	424	0.000				
$B_{1g}(7)$	452		0.020			
$B_{3g}(7)$	457				0.306	
$B_{3u}(7)$	518	0.115				
$B_{1u}(7)$	520	1.776				
$A_g(8)$	535		0.579	1.192	5.887	12.4
$B_{2g}(8)$	541			0.536		
$A_u(8)$	546					
$B_{2u}(7)$	548	0.000				
$B_{3g}(8)$	591				8.965	8.7
$B_{1g}(8)$	593		1.586			
$A_g(9)$	614		6.423	18.540	13.575	4.5
$B_{2g}(9)$	615			0.724		
$B_{3u}(8)$	640	0.618				
$A_u(9)$	668					
$B_{2u}(8)$	670	1.277				
$B_{3g}(9)$	675				0.475	
$B_{1g}(9)$	675		0.023			
$B_{1u}(8)$	706	0.000				

them has an appreciable Raman intensity. More on the displacement pattern of the different modes is given in Sec. IV D where the Raman spectra of the three phases are compared.

D. Comparison of Raman spectra of the three phases

In this section, we discuss the assignment of the experimental Raman peaks to specific phonons and compare the displacement patterns of these phonons in the three different phases. First, we must say that the *ab initio* results presented here are overall in good agreement with previous results from lattice dynamics calculations with empirical interatomic potentials.[7,8,10,11] The displacement patterns of the phonons responsible for the main Raman peaks of α-, β-, and γ-TeO_2 are reported in Figs. 16–18.

As pointed out in Refs. 7 and 11 the Γ-point phonons of α-TeO_2 can be interpreted in terms of the vibrations of the TeO_2 molecule given in Table I. The modes $A_1(4)$ and $B_1(5)$ responsible for the strong Raman peak at 598 cm^{-1} and the weak peak at 537 cm^{-1} (cf. Fig. 13) correspond to symmetric and antisymmetric stretching modes of the TeO_2 molecular

TABLE XI. Theoretical phonon frequencies of γ-TeO_2 at the Γ point, oscillator strengths [f_j in Eq. (4)] of IR-active modes and squared coefficients of the Raman tensor of the Raman-active modes (in units of 10^{-3} Å^3; see Sec. IV). The contribution of the inner longitudinal macroscopic field is not included (LO-TO splitting). All the theoretical values correspond to calculations with the BLYP functional at the experimental lattice parameters. The phonon half-linewidths ($\Delta\omega$) are obtained by fitting the experimental Raman spectra of a polycrystalline sample (Ref. 7) with a sum of Lorentzian functions (Fig. 13).

Mode	ω (cm^{-1})	f_j	a^2 (d^2)	b^2 (e^2)	c^2 (f^2)	$\Delta\omega$
$A(1)$	52		0.029	0.813	0.137	
$B_2(1)$	90	8.215		0.002		
$B_3(1)$	111	0.549			0.084	
$A(2)$	122		2.222	1.502	0.025	4.2
$B_1(1)$	135	0.307	1.190			3.7
$B_1(2)$	137	1.627	1.242			3.7
$B_2(2)$	142	0.069		0.076		
$A(3)$	158		0.693	0.612	2.512	4.5
$B_3(2)$	164	0.144			0.000	
$A(4)$	169		1.138	2.259	2.875	4.5
$B_3(3)$	183	5.049			0.003	
$B_2(3)$	200	0.141		0.117		
$B_1(3)$	201	1.362	0.017			
$A(5)$	212		0.311	0.455	0.112	
$B_3(4)$	265	0.517			0.264	
$B_2(4)$	275	1.935		0.323		
$B_1(4)$	280	2.097	0.457			
$A(6)$	291		0.480	0.529	0.004	
$B_3(5)$	293	2.036			0.661	
$B_1(5)$	305	0.037	0.387			
$B_2(5)$	353	0.608		0.040		
$A(7)$	410		1.467	0.794	29.271	13.4
$B_1(6)$	414	1.670	0.601			
$B_2(6)$	415	3.866		0.257		
$B_3(6)$	496	0.895			0.119	
$A(8)$	575		0.033	0.151	9.968	12.4
$B_1(7)$	585	1.519	0.231			
$B_2(7)$	633	1.147		0.006		
$A(9)$	636		10.494	16.807	3.977	8.7
$B_3(7)$	657	0.577			0.036	
$B_3(8)$	699	0.158			0.026	
$B_2(8)$	737	0.088		0.007		
$B_1(8)$	768	0.005	1.955			4.5

units [Figs. 16(c) and 16(d)]. The mode $A_1(3)$ responsible for the Raman peak at 383 cm^{-1} (Fig. 13) is a bending mode of the TeO_2 molecule [Fig. 16(b)]. The mode $E(6)$ responsible for the weak Raman peak at 336 cm^{-1} is a librational mode of the TeO_2 molecule which modulates the lengths of the two axial bonds [Fig. 16(a)]. The Raman peaks at lower frequencies (120–150 cm^{-1}) are due to librational modes of the TeO_4 units [$E(1)$, $A_1(1)$, and $B_2(1)$ in Table VIII]. The displacement patterns shown in Fig. 16 are in good agreement with those of the corresponding modes obtained in Refs. 7 and 11 from lattice dynamics calculations with empirical interatomic potentials. However, the relative Raman intensities are better reproduced by our *ab initio* calculations than by the bond-polarizability model (BPM) used in Refs. 7 and 11.

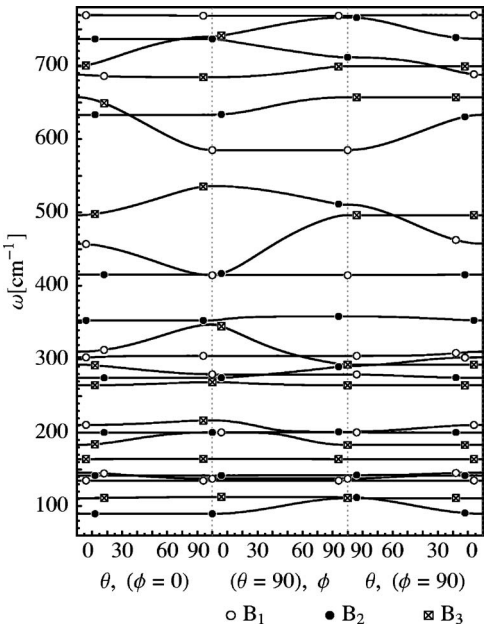

FIG. 15. Angular dispersion of IR-active modes of γ-TeO_2.

Concerning β-TeO_2, the mode $B_{3g}(8)$ responsible for the Raman peak at 591 cm^{-1} is an antisymmetric stretching mode of the TeO_2 molecular unit [Fig. 17(c), in agreement with Refs. 7 and 11]. The mode $A_g(9)$ responsible for the Raman peak at 614 cm^{-1} is instead a stretching mode of just one (the shorter) of the two equatorial bonds [Fig. 17(d)]. The mode $A_g(8)$ at 535 cm^{-1} is the stretching mode of the other longer equatorial bond [Fig. 17(b)]. This is in contrast with the results of lattice dynamics calculations with empirical potentials of Refs. 7 and 11, which give a mixing of the two modes to produce a symmetric and antisymmetric stretching mode of the TeO_2 molecule. The mode $A_g(7)$ at 404 cm^{-1} is a vibration of the Te_2O_2 ring which modulates the length of the axial bonds, in agreement with Refs. 7 and 11. However, the bond-polarizability model used in Refs. 7 and 11 gives unsatisfactory results for the relative Raman intensities.

Concerning γ-TeO_2, the Raman peaks at 636 and 768 cm^{-1} correspond to stretching modes of the shortest Te-O bond in phase [$A(9)$] or out of phase [$B_1(8)$] within the four TeO_2 molecules in the unit cell, respectively [Figs. 18(c) and 18(d)]. The modes $A(8)$ and $A(7)$ responsible for the Raman peaks at 575 and 410 cm^{-1} are mixed stretching and bending modes of the Te-O2′-Te′ bridge with the Te atoms fixed [Figs. 18(a) and 18(b)]. Again, the displacement pattern of these modes are in good agreement with those calculated in Refs. 7 and 11 from empirical interatomic potentials. The analysis of the vibrational spectra of α-TeO_2 and β-TeO_2, presented above, identifies clearly the TeO_2 molecules as the building units of the crystal. How-

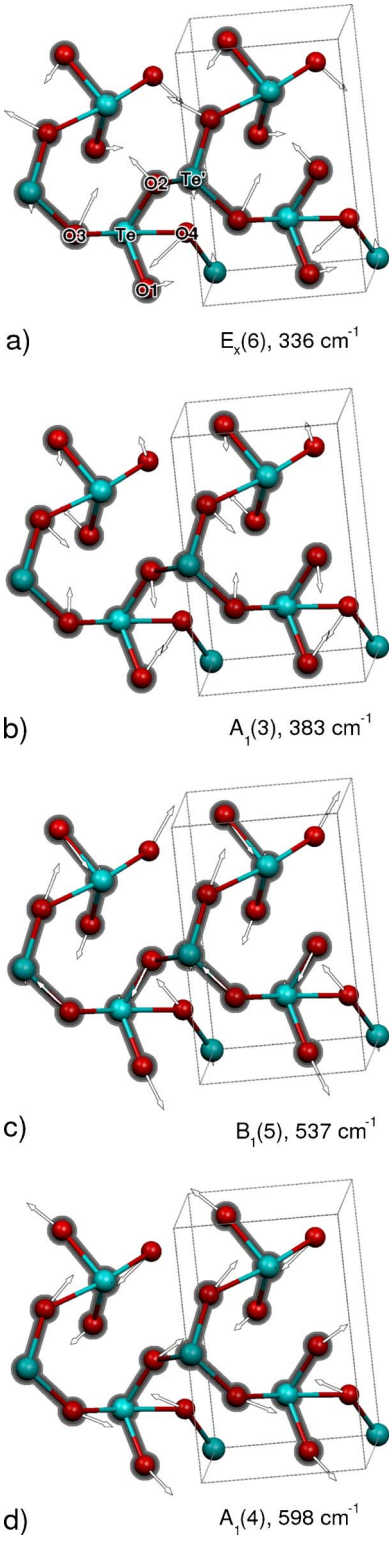

FIG. 16. (Color online) Displacement pattern of the phonons responsible for the main Raman peaks of polycrystalline α-TeO_2 (cf. Fig. 13). The TeO_2 molecules formed by the two shorter equatorial bonds are shadowed.

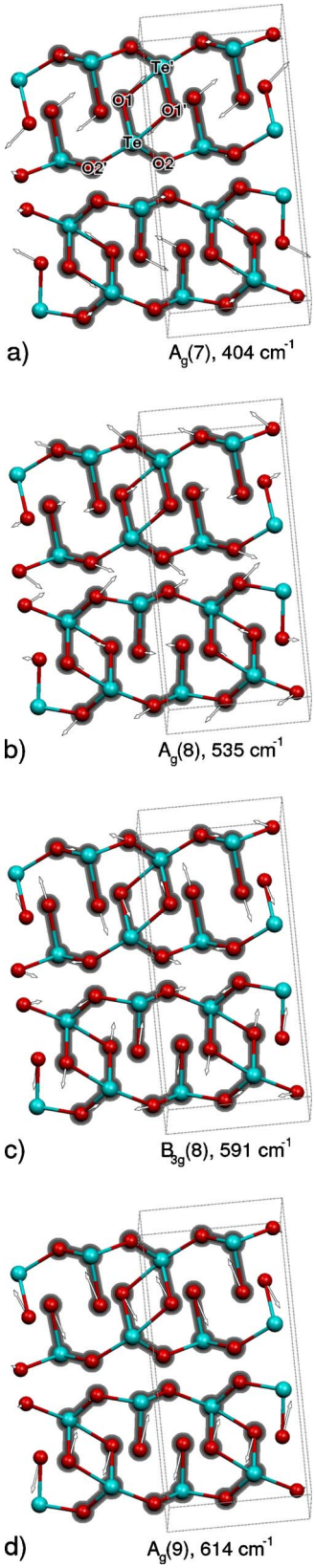

FIG. 17. (Color online) Displacement pattern of the phonons responsible for the main Raman peaks of polycrystalline β-TeO_2 (cf. Fig. 13). The TeO_2 molecules formed by the two shorter equatorial bonds are shadowed.

ever, the interaction between the molecules is large. For instance, the symmetric stretching modes of the TeO_2 unit shift from 598 cm^{-1} [$A_1(4)$] to 726 cm^{-1} [$B_2(4)$] depending on the phase relation between the motion of the different molecules.

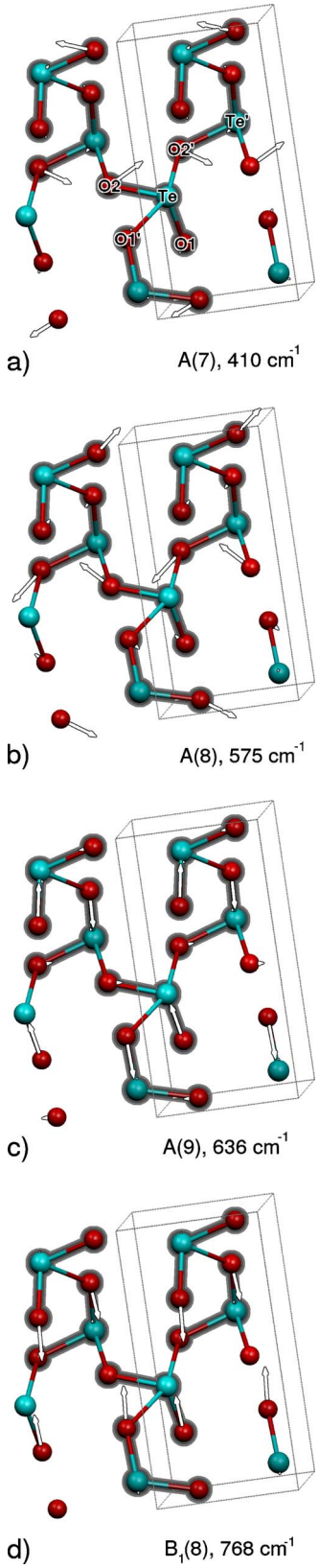

FIG. 18. (Color online) Displacement pattern of the phonons responsible for the main Raman peaks of polycrystalline γ-TeO_2 (cf. Fig. 13). The TeO_2 molecules formed by the two shorter equatorial bonds are shadowed.

As pointed out in Refs. 7 and 11, the γ-TeO_2 phase behaves differently with respect to α- and β-TeO_2 concerning the vibrational properties. Indeed, the displacement patterns reported in Fig. 18 suggest a chainlike structure, the most intense Raman peaks consisting of stretching modes of the Te-O2′-Te′ bridge and of the shortest Te-O bond which might be seen as a side group of the polymeric chain. Still, the chains are strongly interacting since the $A(9)$ and $B_1(8)$ modes, which consist of the same intrachain vibration with different interchain phase relation, differ in frequency by as much as 130 cm^{-1}. We note that in the β phase the lowest-energy phonons [$A_u(1)$, $B_{3u}(1)$, $B_{1u}(1)$ at 38–55 cm^{-1}] correspond to rigid out-of-phase translational modes of the two layers in the unit cell. In γ-TeO_2, the lowest mode at 52 cm^{-1} corresponds to a rigid translation of the chains along the chain axes, out of phase between the two chains in the unit cell. The other two modes at higher frequency (80 and 111 cm^{-1}) involve instead sizable deformations of the chains themselves. In α-TeO_2 the low-frequency modes (below 140 cm^{-1}) can be well described as rigid motions of the TeO_4 units around the bridging oxygen atoms.

V. CONCLUSIONS

Based on first-principles calculations, we have studied the structural and vibrational properties of the three crystalline phases of TeO_2 (α, β, γ). Phonon dispersion relations and IR and Raman spectra have been computed within density functional perturbation theory. The calculated Raman and IR spectra are in good agreement with available experimental data, and with previous lattice dynamics calculations based on empirical interatomic potentials,[7,8,10,11] but for an underestimation of the frequency of the Te-O stretching modes (above 500 cm^{-1}). The modes at high frequency (400–800 cm^{-1}) can be well described in terms of vibrations of TeO_2 molecular units in α- and β-TeO_2 which would then be seen as molecular crystals. The analysis of the vibrational spectrum of γ-TeO_2 suggests instead a stronger intermolecular interaction supporting the picture of γ-TeO_2 as a chainlike structure, more connected than α- and β-TeO_2. However, the calculated elastic constants and electronic band structure do not show strong anisotropies, which would have been expected from the description of γ-TeO_2 as the assembling of aligned polymers proposed experimentally. As a matter of fact, TeO_2 molecules in α- and β-TeO_2 and polymerized TeO_2 chains in γ-TeO_2 are strongly interacting, possibly via electrostatic coupling, as suggested by the strong ionic character of the Te-O bond emerging from previous *ab initio* calculations.[21,25]

ACKNOWLEDGMENTS

This work is partially supported by the INFM Parallel Computing Initiative. Discussions with G. Dai and F. Tassone are gratefully acknowledged.

[1] R. A. H. El-Mallanwany, *Tellurite Glasses Handbook* (CRC Press, Boca Raton, FL, 2002).
[2] D. Dai, F. Tassone, A. Li Bassi, V. Russo, C. E. Bottani, and D. D'Amore, IEEE Photonics Technol. Lett. **16**, 1011 (2004).
[3] C. Rivero, K. Richardson, R. Stegeman, G. Stegeman, T. Cardinal, E. Fargin, M. Couzi, and V. Rodriguez, J. Non-Cryst. Solids **345&346**, 396 (2004).
[4] P. A. Thomas, J. Phys. C **21**, 4611 (1988).
[5] V. H. Beyer, Z. Kristallogr. **124**, 228 (1967).
[6] S. Blanchandin, P. Marchet, P. Thomas, J. C. Champarnaud-Mesjard, and B. Frit, J. Mater. Chem. **9**, 1785 (1999).
[7] J. C. Champarnaud-Mesjard, S. Blanchandin, P. Thomas, A. P. Mirgorodsky, T. Merle-Mejean, and B. Frit, J. Phys. Chem. Solids **61**, 1499 (2000).
[8] O. Noguera, T. Merle-Mejean, A. P. Mirgorodsky, M. Smirnov, P. Thomas, and J. C. Champarnaud-Mesjard, J. Non-Cryst. Solids **330**, 50 (2003).
[9] N. Kimura, and T. Sato, J. Phys. Soc. Jpn. **63**, 3704 (1994).
[10] A. P. Mirgorodsky, T. Merle-Mejean, J. C. Champarnaud-Mesjard, and B. Frit, J. Phys. Chem. Solids **61**, 1499 (2000).
[11] O. Noguera, Ph.D. thesis, University of Limoges, 2003, http://www.unilim.fr/scd/
[12] J. P. Perdew, K. Burke, and M. Ernzerhof, Phys. Rev. Lett. **77**, 3865 (1996).
[13] A. D. Becke, Phys. Rev. A **38**, 3098 (1988); C. Lee, W. Yang, and R. G. Parr, Phys. Rev. B **37**, 785 (1988).
[14] S. Baroni, A. dal Corso, S. de Gironcoli, and P. Giannozzi, http://www.pwscf.org
[15] D. Vanderbilt, Phys. Rev. B **41**, 7892 (1990).
[16] H. J. Monkhorst and J. D. Pack, Phys. Rev. B **13**, 5188 (1976).
[17] D. Murnaghan, Proc. Natl. Acad. Sci. U.S.A. **30**, 224 (1944).
[18] S. Baroni, S. de Gironcoli, A. Dal Corso, and P. Giannozzi, Rev. Mod. Phys. **73**, 515 (2001).
[19] N. Troullier, and J. L. Martins, Phys. Rev. B **43**, 1993 (1991).
[20] H. Ogi, M. Fukunaga, M. Hirao, and H. Ledbetter, Phys. Rev. B **69**, 024104 (2004).
[21] B. R. Sahu and L. Kleinman, Phys. Rev. B **69**, 193101 (2004).
[22] *Handbook of Chemistry and Physics*, 84th ed., edited by D. R. Lide (CRC Press, Boca Raton, FL, 2004).
[23] The calculated (PBE) bond lengths and vibrational frequencies of O_2 and Te_2 in the triplet states are, respectively, O_2, $d=1.254$ Å (expt. 1.208 Å), $\omega=1570$ cm^{-1} (expt. 1580.2 cm^{-1}); Te_2, $d=2.584$ Å (expt. 2.557 Å), $\omega=247$ cm^{-1} (expt. 247.1 cm^{-1}). Experimental values are from Ref. 22.
[24] T. G. Worlton and R. A. Beyerlein, Phys. Rev. B **12**, 1899 (1975).
[25] E. Menendez-Proupin, G. Gutierrez, E. Palmero, and J. L. Pena, Phys. Rev. B **70**, 035112 (2004).
[26] R. Claus, Phys. Status Solidi B **100**, 9 (1980).
[27] *Light Scattering in Solids II*, edited by M. Cardona, and G. Güntherodt (Springer-Verlag, Berlin, 1982).
[28] P. Brüesch, *Phonons: Theory and Experiments II* (Springer-Verlag, Berlin, 1986).
[29] D. M. Korn, A. S. Pine, G. Dresselhaus, and T. B. Reed, Phys. Rev. B **8**, 768 (1973).
[30] N. N. Syrbu and R. V. Cretu, Infrared Phys. Technol. **37**, 769 (1996).
[31] R. Loudon, Adv. Phys. **50**, 813 (2001).
[32] See EPAPS Document No. E-PRBMDO-73-050610 for derivatives of dielectric tensor with respect to the displacement of symmetry-independent atoms. This document can be reached via a direct link in the online article's HTML reference section or via the EPAPS homepage (http://www.aip.org/pubservers/epaps.html).
[33] A. S. Pine and G. Dresselhaus, Phys. Rev. B **5**, 4087 (1972).
[34] O. Noguera, M. Smirnov, A. P. Mirgorodsky, T. Merle-Mejean, P. Thomas, and J. C. Champarnaud-Mesjard, Phys. Rev. B **68**, 094203 (2003).
[35] M. Spoliti, S. Cesaro, and E. Coffari, J. Chem. Thermodyn. **4**, 507 (1972).